

Room-temperature I – V characteristics of a single hollow $\text{La}_{2/3}\text{Ca}_{1/3}\text{MnO}_3$ microparticle

M E Saleta^{1,2,3}, M Granada^{1,3,4}, J Curiale^{1,3,4}, R Benavides¹,
H E Troiani^{1,2,3} and R D Sánchez^{1,2,3}

¹ Centro Atómico Bariloche, Comisión Nacional de Energía Atómica, Avenida Bustillo 9500, 8400 S.C. de Bariloche, RN, Argentina

² Instituto Balseiro, Comisión Nacional de Energía Atómica and Universidad Nacional de Cuyo, Avenida Bustillo 9500, 8400 S.C. de Bariloche, RN, Argentina

³ Consejo Nacional de Investigaciones Científicas y Técnicas—CONICET, CCT-Comahue, Quintral 1250, 8400 S.C. de Bariloche, RN, Argentina

⁴ Laboratoire de Photonique et de Nanostructures, CNRS, F-91460 Marcoussis, France

E-mail: rodo@cab.cnea.gov.ar (R D Sánchez)

Received 1 February 2011, in final form 17 May 2011

Published 15 June 2011

Online at stacks.iop.org/JPhysCM/23/275301

Abstract

In this work we present an electrical characterization of $\text{La}_{2/3}\text{Ca}_{1/3}\text{MnO}_3$ particles obtained by spray pyrolysis. We optimized the synthesis conditions to obtain the desired compound with the expected structure and the ferromagnetic transition at the same temperature as the bulk material. We found that a post-deposition thermal treatment enhances the magnetic properties of the samples. The study of structural, morphological and magnetic properties shows that the walls of the hollow spheres are constituted by grains on the nanometer scale. The I – V characterization shows typical signatures of tunneling transport. This behavior can be associated with the grain boundaries within the microparticle's wall acting as tunnel barriers.

(Some figures in this article are in colour only in the electronic version)

1. Introduction

The reduction of a material's size to the nanoscale has given rise to the discovery of novel phenomena that differ from the properties of the bulk material and that have been of great interest for basic and technological reasons. In the last decade an important effort of the scientific community has been oriented to prepare and characterize nanomaterials with wire, tubular, ribbon and spherical geometries.

In previous works our group has studied $\text{La}_{2/3}\text{Ca}_{1/3}\text{MnO}_3$ (LCMO) manganite nanotubes, nanowires and nanograins, and we found that the magnetic properties of the samples are strongly correlated with their morphology [1, 2]. The ferromagnetic LCMO polycrystalline samples present properties such as a large low-field magnetoresistance (LFMR), due to the existence of the grain boundaries, and this effect is enhanced in nanocrystalline samples [1]. The study of the current–voltage (I – V) curves shows a nonlinear behavior explained by the tunneling model and associated

with the grain boundary insulating barriers [3]. In the case of LCMO nanotubes, we found that they are constituted by the agglomeration of nanograins of the material. The tubular nanostructures present a lower T_C ($T_C^{\text{NT}} = 258$ K) [2] than the bulk material ($T_C^{\text{Bulk}} = 273$ K) but close to the nanograins ($235 \text{ K} < T_C^{\text{NP}} < 250 \text{ K}$) [1]. The nanograins that form the nanotubes present a surrounding non-crystalline shell of 2 nm, which is a magnetic dead layer and was described in [4].

LCMO films or particles are ideal for interesting applications such as solid oxide fuel cells [5–7], magnetic field sensors [8] and electronic devices [9, 10]. Also the granular ferromagnetic films of LCMO synthesized by spray pyrolysis present LFMR [11].

The spray-pyrolysis method is one of the most appropriate for fabricating spherical microparticles of oxides [12–14]. The synthesis method consists in spraying a solution of the precursors for obtaining a given compound onto a heated substrate or into a heated reaction chamber. The high temperature causes a chemical reaction to occur and the

remaining components of the solution to evaporate. The characteristics and shape of the samples (i.e. films or particles) are the result of several instrumental parameters (temperature gradient, type of nozzle, nozzle–substrate or nozzle–chamber distance), the solution (pH, concentration of precursors, surface tension, etc) and synthesis atmosphere. This method is fast and inexpensive compared with other deposition techniques, and it has been proved to allow for the fabrication of high quality samples [15, 16].

For this work we synthesized microparticles of a ferromagnetic LCMO manganite by spray pyrolysis at different temperatures and studied their morphology and magnetic properties as deposited and after thermal treatment. To study the electrical transport properties of our samples, we performed an I – V characterization of single microparticles inside a scanning electron microscope chamber with a nanomanipulation system. We explained the results in terms of a tunneling model based on the granular structure of the wall of our hollow microparticles. Parameters such as the height and width of the average tunnel barrier have been estimated.

2. Experimental techniques

The samples were deposited in a home-made spray-pyrolysis equipment. The spray was produced with a Sono-Tek ultrasonic nozzle system [17] with a frequency of 48 kHz, placed on top of the reactor chamber, which is constituted by a quartz tube in a vertical configuration. The liquid feeding rate during the experiments was approximately 0.08 ml s^{-1} . The microparticles were collected onto (001) Si substrates in the center of the reactor and placed at 45 cm from the ultrasonic nozzle, where the temperature was set by a tubular furnace equipped with a temperature controller. The temperature of the substrates was measured with an S-type thermocouple placed in the substrate holder. To obtain the $\text{La}_{2/3}\text{Ca}_{1/3}\text{MnO}_3$ (LCMO) manganite, we prepared an aqueous solution of high purity La, Ca and Mn nitrates. The precursors, in the proportions $\text{La}:\text{Ca}:\text{Mn} = 2:1:3$, were dissolved in twice-distilled water and magnetically stirred to homogenize the solution. The resulting solution had a 0.2 M concentration and pH close to 6. Before each deposition, the solution was ultrasonicated to improve the homogenization. The deposition procedure was carried out in air, without any additional gas flow.

The morphological characterization was performed by transmission and scanning electron microscopy (TEM and SEM). TEM images were obtained with a Philips CM 200 microscope, equipped with an ultratwin lens, operated at 200 kV. The SEM micrographs were acquired with a Philips XL30 and a Philips 515 microscope with an EDAX probe for energy-dispersive spectroscopy (EDS). The structure of the samples was studied by x-ray powder diffraction (XRD) at room temperature with a Philips PW1700 diffractometer, using $\text{Cu K}\alpha$ radiation ($\lambda_\alpha = 1.5418 \text{ \AA}$). The cell parameters were calculated from XRD data by the Rietveld method using the Fullprof code [18].

The dc magnetic behavior was studied by a superconducting quantum interference device magnetometer (Quantum

Design MPMS-5S). The magnetization (M) as a function of temperature (T) was measured in the range $5 \text{ K} \leq T \leq 300 \text{ K}$, with an external magnetic field $H = 100 \text{ Oe}$. The measurements, as a function of H , were performed at $T = 5 \text{ K}$ in the range $-50 \text{ kOe} \leq T \leq 50 \text{ kOe}$.

The current–voltage (I – V) curves of isolated spherical microparticles were measured inside the XL30 SEM chamber with a Keithley 4200-SCS (semiconductor characterization system) connected to a Zyvex sProber Nanomanipulation System, using a two-point technique. The nanomanipulator system allows us to move up to four different tungsten tips, with 2 nm resolution. Before measuring the I – V curves, the microscope chamber with the stage and the sample inside are cleaned with a Zyvex Optimizer Unit which produces an oxygen plasma to clean the hydrocarbon contamination. Also to avoid oxide coating on the tips, before the measurement we cross the two tips and increase the electrical current in steps until we reach a resistance of around 20Ω between the tips.

3. Results and discussion

3.1. Synthesis and structural characterization

Three samples were deposited at different initial substrate temperatures: 953 K (sA), 748 K (sB) and 537 K (sC). When the spray is produced, it progressively cools down the system, making the temperature of the reactor, and therefore of the substrate, vary in time. In order to keep the substrate at a nearly constant temperature, the deposition was performed in five steps of 2 min, separated by 2 min gaps between them for the system to recover its initial temperature. In the case of sA and sB, while the spray was produced the temperature of the substrates dropped by about 25° , but during the waiting times they recovered the initial temperature. In the case of sC, the 2 min waiting time was not enough: the substrate was cooled down by 120 K during this procedure. After deposition, in order to achieve the perovskite phase, the samples were held at 953 K for 30 min and then cooled down slowly to room temperature. The temperature profiles during the whole deposition procedures for all the samples are presented in figure 1(a). Regarding the chemical composition, EDS analysis indicates that sA and sB have the correct stoichiometry, while sC is Mn-rich. So the deposition at low temperatures should be optimized in order to obtain the desired compound.

A comparison between the morphology of the three samples is shown in figures 1(b)–(d).

SEM images show that all of them present spherical structures with a wide size dispersion. In sample sA the spheres lie on the Si substrate, while in sB a cracked LCMO layer completely covers the substrate and the microparticles are deposited on top. Finally, in sC the microparticles are much more agglomerated, forming a more compact material. We note that the density of microparticles is larger when the deposition temperature is lower. We found that all the studied microparticles are hollow. Some of them were already broken after deposition, while others that were initially spherical were broken using the nanomanipulator's tips. In figure 2(a) a typical broken hollow microparticle is shown.

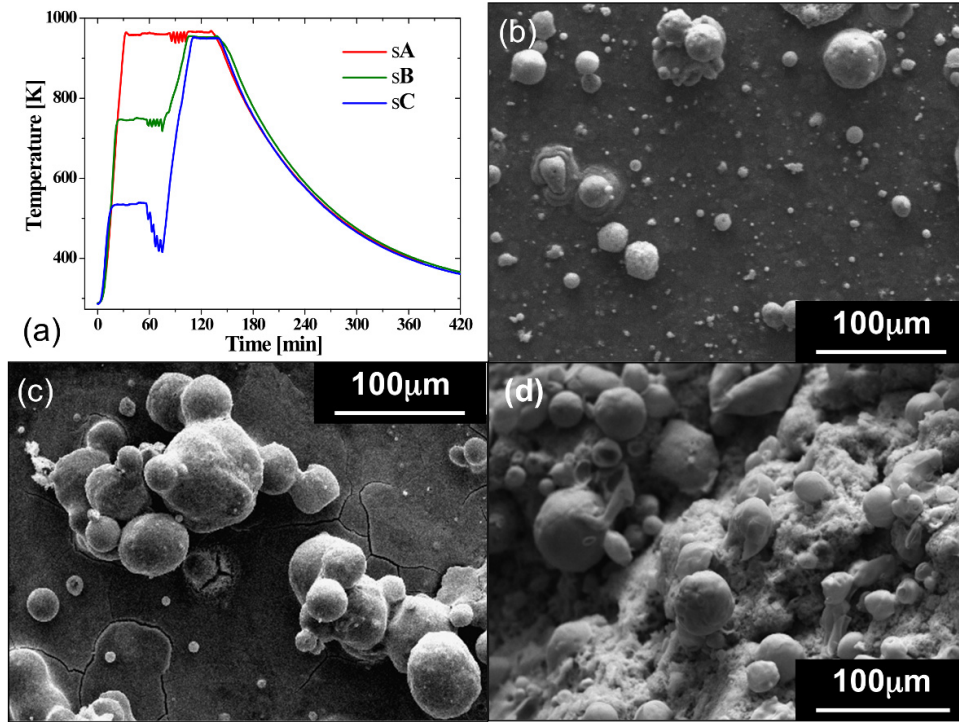


Figure 1. (a) Substrate temperature during the synthesis process as detailed in the text. SEM images of (b) sA, (c) sB and (d) sC.

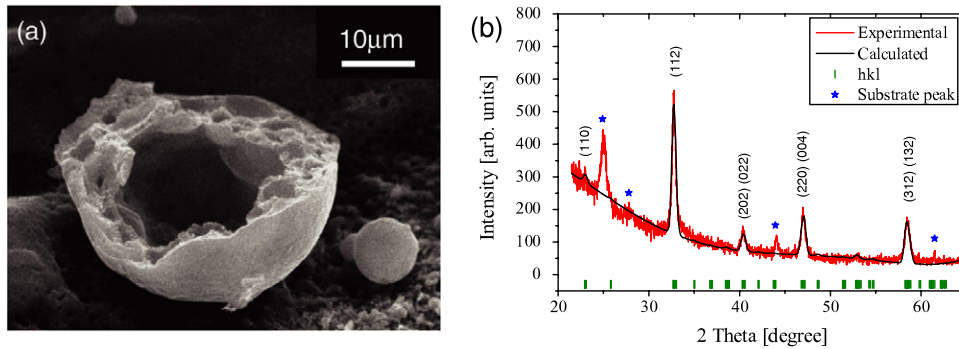


Figure 2. (a) SEM micrograph of a broken hollow microparticle. (b) XRD pattern of sB fitted using the Rietveld method; reflections coming from the substrate are indicated by stars.

These microparticles are highly porous, they have varying diameters and wall thicknesses, and we have observed bubbles within the walls. The fit of the XRD data indicates that sA and sB crystallized in the $Pbnm$ space group and the refined parameters are in good agreement with those reported in the references for bulk LCMO [19]. In figure 2(b) we show a typical XRD profile with the LCMO peaks and the extra reflections coming from the substrate. The crystallite size for sA and sB, (11.5 ± 0.7) nm, was determined by using the Scherrer formula [20].

In order to study the microstructure of the particles' walls we performed a TEM characterization. In figure 3 we observe that the particles are composed of nanometer-sized crystallites. In the bright-field TEM image of figure 3(a) we observe a grain-size distribution between 10 and 50 nm with an average diameter of $d = 25$ nm. High resolution TEM images show that the samples present good crystallinity (figure 3(b)); the

selected-area electron diffraction (SAED) pattern (figure 3(c)) confirms this fact and it also shows that the crystallites are randomly oriented.

Based on the information obtained from the structural characterization, we propose a simplified representation of the microparticles that takes into account the main characteristics. We show in figure 4 a schematic picture of a hollow microparticle with diameter D and wall thickness δ_w . The wall is composed of nanoparticles of diameter d which consist of a crystalline core and an amorphous shell. This picture will be used in the section when discussing the I - V results.

3.2. Magnetization and thermal treatment

We performed a magnetic characterization of sA and sB. We found that, even though the shape of the $M(T)$ curves is different from the bulk material, the T_C is the expected one.

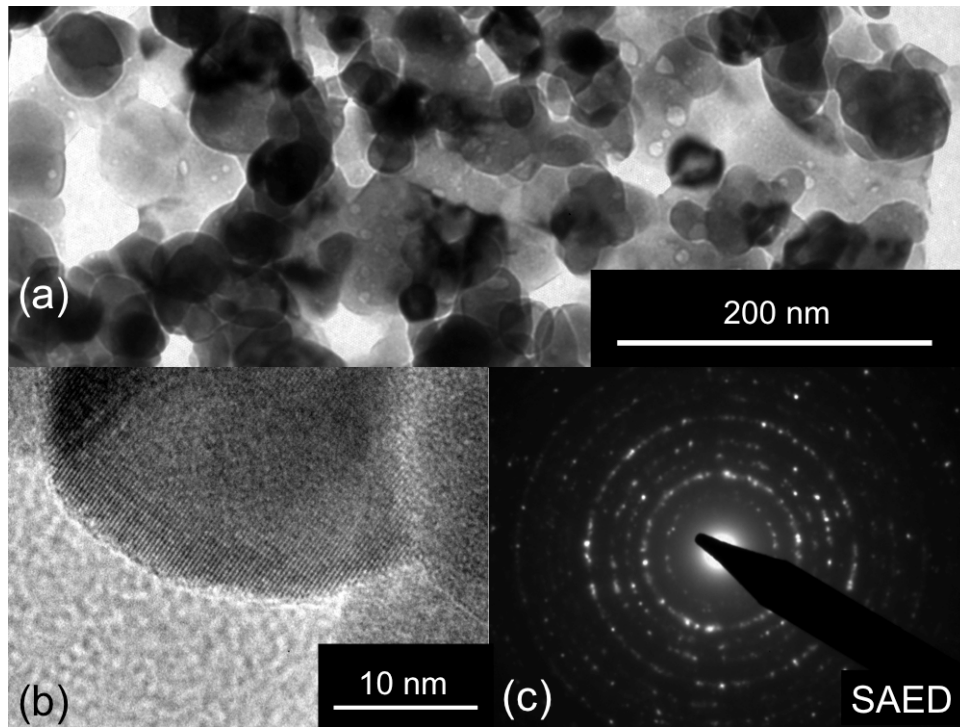


Figure 3. (a) Bright-field TEM image of the nanograins that constitute the walls of **sB** microspheres. (b) High resolution TEM image of a nanometric crystallite of the sample **sB**. (c) SAED pattern of **sB**.

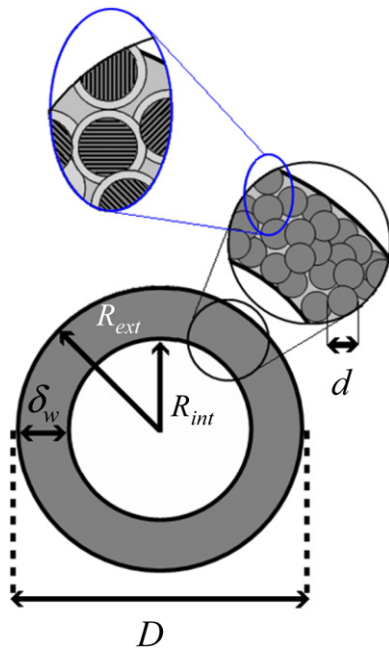


Figure 4. Schematic picture of a hollow microparticle with diameter D and wall thickness δ_w . A first zoom shows the detail of the nanograins of diameter d that constitute the wall of the microsphere and a second zoom of this area shows the core (crystalline)–shell (amorphous) structure of the nanograins.

In order to improve the magnetization, we performed an extra thermal treatment (TT) consisting in heating the samples from room temperature up to 923 K in 1.5 h, annealing at that temperature for 5 h and then cooling down slowly to room

temperature. In figure 5 we compare the $M(T)$ measurements for **sA** and **sB**, as deposited and after the TT. In both samples the magnetization increases after the TT. In the case of **sA**, the shape of the $M(T)$ curve after TT approaches that of the bulk, this reflecting a qualitative improvement of the magnetic properties by the TT.

In figure 6 we show the magnetization as a function of the magnetic field measured at 5 K. The inset shows a detail of the hysteresis loop where a large coercive field $H_c \sim 400$ Oe and a normalized remanence close to 0.5 are observed. This curve is similar to those measured for nanotubes, whose walls are also constituted by nanograins of the same size as those of the microparticles [2, 4].

SEM images indicate that the morphology of the microparticles does not change noticeably with the TT. Nevertheless, XRD patterns show a narrowing of the LCMO peaks. In particular, for the reflection at $2\theta = 59^\circ$, we observe that the peak width of the as-made sample, (0.0138 ± 0.0008) rad, decreases to (0.0112 ± 0.0006) rad after annealing. By applying the Scherrer equation we have calculated the crystallite size, obtaining (11.5 ± 0.7) nm and (14.2 ± 0.7) nm, respectively. This indicates an increase in the crystallite size of 22%, which is consistent with the observed improvement of magnetization. However, there exist additional effects which could also contribute to the narrowing of the XRD peaks and to the improvement of the sample's crystalline quality after the TT, i.e. by reducing microstrains or defects, or by reducing the disorder at the grain boundaries; any of these modifications would also result in an increase of the magnetization. Finally, the $M(T)$ curves show a small increase at low temperatures,

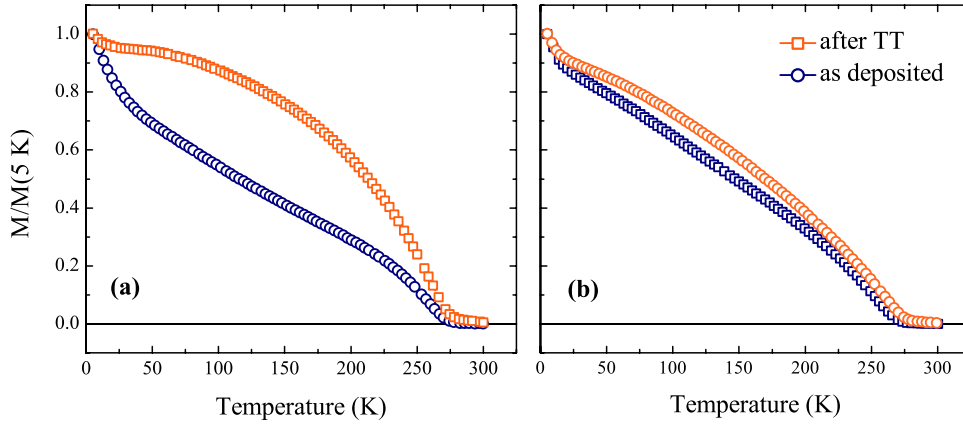


Figure 5. Magnetization versus temperature for sA (a) and sB (b) as deposited and after the TT. The magnetization was measured with $H = 100$ Oe after saturating the samples at 5 K.

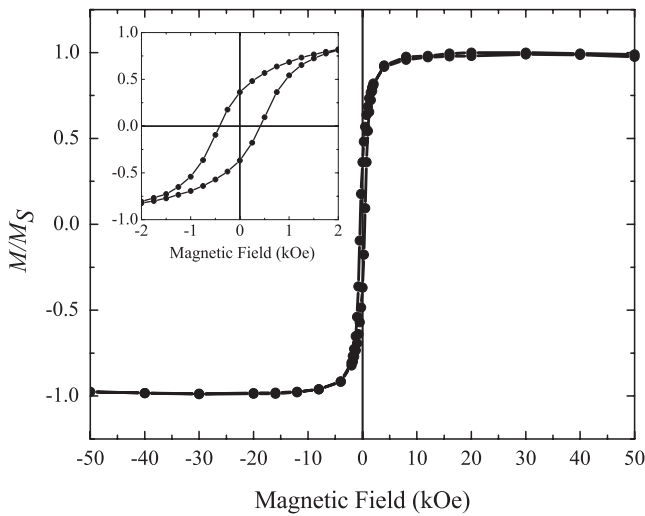


Figure 6. Normalized magnetization with respect to the saturation magnetization as a function of magnetic field of the sA sample. Inset: detail of the hysteresis loop at low magnetic field to appreciate the coercive magnetic field.

which can be associated with nanograins with a very small crystallite size presenting superparamagnetic behavior.

3.3. I - V experimental results

The current-voltage (I - V) characterization was performed on more than ten microspheres of sample sA-TT. We focused on this sample for two reasons: first, because by using this synthesis protocol we obtained isolated single spherical microparticles dispersed onto the silicon substrate and, second, because the magnetic properties are those expected for LCMO granular systems. In figure 7(a) we present a SEM micrograph of a spherical microparticle with a $13.3 \mu\text{m}$ diameter and three tungsten tips in mechanical contact with the microparticle surface.

The I - V curves were measured by using two tips, labeled P1 and P3 in figure 7(a). We applied a linear voltage ramp from 0 to 6 V between the tips, thus obtaining current values

of some μA . To verify that we have a good electrical contact and that there are no current leaks, we measured the current in each tip independently and we checked that the magnitude and dependence of the current is the same in both tips. The current as a function of voltage for both tips is shown in figure 7(b), where the curves are completely symmetric and present non-ohmic behavior.

When electronic transport occurs via tunneling through an insulating barrier, the I - V curves as a function of V can be written in the form

$$J/V = a_0 + a_1 V^2 \quad (1)$$

where J is the current per unit area. We estimate $J = I/A$ using the area A of the equatorial ring. In figure 8, J/V as a function of V^2 is presented, the experimental data are shown in circles and the solid line corresponds to the fit by using equation (1). The obtained parameters are $a_0 = (0.3 \pm 0.1) \Omega^{-1} \text{cm}^{-2}$ and $a_1 = (0.42 \pm 0.01) \Omega^{-1} \text{cm}^{-2} \text{V}^{-2}$. The inset plot shows the total electrical conductance ($G_T = J/V$) of the microsphere as a function of V .

It is important to note that, unlike a previous work [3], where the nonlinear I - V curves were measured at low temperature, in the present work the experiments were performed at room temperature. In order to analyze the results, we also assume that the potential drop occurs mainly in the grain boundaries, composed by an amorphous layer, that act as tunnel barriers between the crystalline grains. It has been demonstrated that the room-temperature resistivity of polycrystalline manganite samples strongly depends on the grain size, giving an increasing resistance when the grain size is reduced [21, 22]. This result proved that the electrical transport at room temperature is also strongly influenced by surface effects.

3.4. Model

Recently, we observed by TEM microscopy a 20 \AA thick crystalline disordered layer on the surface of each nanograin [4]. This layer is the physical origin of a magnetic dead layer and also of the insulating barriers that determine the

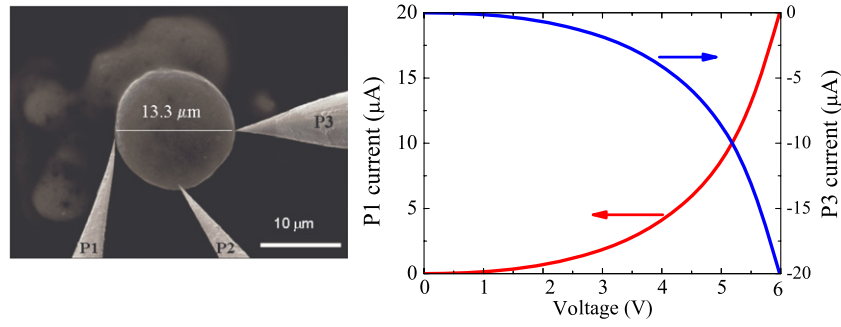


Figure 7. (a) Manganite microsphere of **sA-TT** series in mechanical and electrical contact with the three probes. (b) Current versus voltage measured in the same microparticle.

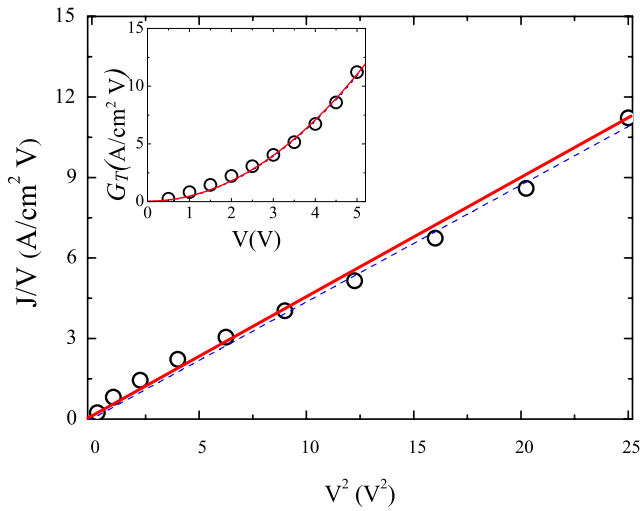


Figure 8. Experimental J/V versus V^2 (circles). In the inset is shown $G_T = J/V$ as a function of voltage. In both panels, the solid line is the result of the linear fit using equation (1). The dashed line is calculated using the tunneling model (as discussed in the text) with parameters $\frac{N_c}{N_b} = 39.5$, $s = 16$ Å and $\varphi \approx 2.6$ eV.

electrical transport properties of these individual objects. Note that at room temperature the LCMO samples are paramagnetic and consequently it is not necessary to consider a magnetic barrier due to the misalignment of the magnetizations of neighboring nanograins. In this case the origin of the tunnel barriers is strictly due to structural disorder as discussed in [3]. The model should include the consideration that all the grain boundaries act as tunnel barriers affecting the conductance. This is coherent with the measured resistance values and the poor cohesion between the nanograins that allows us to break the microparticles' walls by using the nanomanipulator's tips as mentioned before. For the case of a single square tunnel barrier, the Simmons model [23] describes, at low voltages, the current density behavior as

$$g_s(V) = g_0 + g_1 V^2, \quad (2)$$

where g_0 and g_1 are related to the barrier height φ and thickness s through

$$g_0(\beta, s) = \frac{3.1 \times 10^{10}}{s^2} \beta \exp[-\beta] \quad (3)$$

$$g_1(\beta, s) = \left(\frac{1}{192\beta} - \frac{1}{64\beta^2} - \frac{1}{64\beta^3} \right) 6.84 \times 10^{10} s^2 \exp[-\beta] \quad (4)$$

with $\beta = 1.025s\sqrt{\varphi}$. This parameter is associated with the tunnel probability through the insulator barrier and it is called the strength of the barrier. In these formulae g_0 is expressed in $\Omega^{-1} \text{ cm}^{-2}$, g_1 in $\Omega^{-1} \text{ cm}^{-2} \text{ V}^{-2}$, s in Å and φ in eV.

Now, to complete the model, we consider the several barriers that the electrons must go through, from the source to the drain electrode, as serial resistances forming a simple array. The number of barriers N_b can be estimated as the ratio of the distance l from P1 to P3 along the microparticle surface, to the average size of the nanograins that constitute the walls ($d \approx 25$ nm). Then, $N_b = l/d$ with $l = \pi D/2$, where D is the diameter of the microparticle. For the particle in figure 7, we have that $N_b \approx 820$ barriers. Also, it is necessary to take into account that the electrons have several ways to reach the drain electrode and we consider these channels as parallel resistances. The number of channels (N_c) can be estimated as the ratio of the microparticle's cross-section area to the nanograin area. Then $N_c \approx [R_{\text{ext}}^2 - R_{\text{int}}^2]/(d/2)^2 \approx 33\,000$, where $R_{\text{int}} = D/2 - \delta_w$ and $\delta_w \approx 400$ nm (see figure 4 for the definition of the parameters). Taking into account these geometric considerations and the Simmons g_s tunnel conductance for one barrier, the total conductance G_T expected for the microparticle system is

$$G_T(V) = J/V = \sum_{i=1}^{N_c} \frac{g_s(V)}{N_b} = \frac{N_c g_0}{N_b} + \frac{N_c g_1}{N_b} V^2. \quad (5)$$

Comparing equations (1) and (5), the parameters $a_0 = \frac{N_c g_0}{N_b}$ and $a_1 = \frac{N_c g_1}{N_b}$ obtained by fitting the data of figure 8 now acquire a physical meaning. One strategy to find the best description of the system behavior is to take different s values, for example between 15 Å (structural disordered layer obtained in LSMO polycrystalline films) [24] and 40 Å (twice the structural disordered layer thickness observed in nanoparticles of similar diameters to those that form our microsphere) [4]. Then, the only parameter that we need to find in order to complete the description is the barrier height (φ). For each fixed s value, by using equations (2)–(5), we found a φ value (listed in table 1) that acceptably fits the experimental data.

Table 1 also shows the β , a_0 and a_1 parameters calculated for each set (s , φ). Note that all β values are similar, and the

Table 1. Parameters of the model described in the text, obtained by fitting the experimental data for different s values. The bold text highlights the set of parameters that present the minimum χ^2 .

s (Å)	φ (eV)	a_0 ($\Omega \text{ cm}^2$) ⁻¹	a_1 ($\Omega \text{ cm}^2 \text{ V}^2$) ⁻¹	β	χ^2
15	2.9243	0.5458	0.4049	26.2923	0.09
16	2.5914	0.4323	0.4121	26.4003	0.08
20	1.7088	0.1887	0.4271	26.7979	0.27
25	1.1280	0.0808	0.4336	27.2157	0.50
30	0.8035	0.0401	0.4360	27.5638	0.62
35	0.6031	0.0221	0.4371	27.8603	0.69
40	0.4703	0.0132	0.4376	28.1182	0.72

same happens with a_1 (slope of J/V versus V^2 in figure 8). In contrast, a_0 (y intercept of J/V versus V^2) is very sensitive to the s parameter, although its determination has an important error ($\approx 30\%$).

In order to find the most representative set of parameters to describe the experiment, we look for the lowest χ^2 coefficient, also displayed in table 1. This coefficient is defined as $\chi^2 = \sum \frac{((J/V)_E - (J/V)_M)^2}{(J/V)_M}$, where $(J/V)_E$ and $(J/V)_M$ are the experimental and model J/V data, respectively.

The lowest χ^2 value corresponds to $s = 16$ Å and associated parameters, $\varphi = 2.5914$ eV and $\beta = 26.4003$; these values were used to calculate the total conductance of the hollow sphere using equation (5) (dashed curve in figure 8).

The description of the experimental data by using the proposed model shows that a set of $N_c \approx 33\,000$ parallel conducting channels, each of them with $N_b \approx 820$ barriers of width $s = 16$ Å and height $\varphi = 2.5914$ eV, can properly explain the experimental results.

4. Conclusions

We have synthesized LCMO hollow microparticles that have polycrystalline walls formed by nanograins of ~ 25 nm in diameter. We optimized the deposition parameters to obtain samples that present the expected T_C and $M(T)$ behavior of LCMO. We have shown that the magnetic response is enhanced by a thermal treatment, approaching qualitatively that of the bulk material. The room-temperature $I-V$ characterization of a single hollow microparticle prepared by the optimized method presents a nonlinear behavior, associated with tunneling transport. The total electrical conductance G_T can be well described by considering an array of equal grain boundary barriers and using the Simmons model to describe each single barrier conductance. The parameters that best describe our experimental results are $s = 16$ Å and $\varphi \approx 2.6$ eV, yielding a barrier strength $\beta \approx 26.4$. This work contributes to demonstrate that the room-temperature tunneling behavior of the electrical transport properties in these nanostructured

manganites is a potential candidate to build magnetic tunnel junctions, which could be applied in solid-state magnetic random access memory devices.

Acknowledgments

The authors acknowledge J C Pérez for valuable technical assistance. MES acknowledges a CONICET studentship. This work was supported by ANPCyT and CONICET through PME-20 in PAE-37063; UN Cuyo 06/C324 and ANPCyT PICT 2007-0892.

References

- [1] Sánchez R D, Rivas J, Vázquez-Vázquez C, López-Quintela A, Causa M T, Tovar M and Oseroff S 1996 *Appl. Phys. Lett.* **68** 134
- [2] Curiale J, Sánchez R D, Troiani H E, Ramos C A, Pastoriza H, Leyva A G and Levy P 2007 *Phys. Rev. B* **75** 224410
- [3] Niebiskikwiat D, Sánchez R D, Lamas D G and Caneiro A 2003 *J. Appl. Phys.* **93** 6305
- [4] Curiale J, Granada M, Troiani H E, Sánchez R D, Levy P, Leyva A G and Samwer K 2009 *Appl. Phys. Lett.* **95** 43106
- [5] Hamedani H A, Dahmen K-H, Li D, Peydaye-Saheli H, Garmestani H and Khaleel M 2008 *Mater. Sci. Eng. B* **153** 1
- [6] Darbandi A J, Enz T and Hahn H 2009 *Solid State Ion.* **180** 424
- [7] Leyva A G, Curiale J, Troiani H E, Rosenbuch M, Levy P and Sánchez R D 2006 *Adv. Sci. Technol.* **51** 54
- [8] Xu Y, Memmert U and Hartmann U 2001 *Sensors Actuators A* **91** 26
- [9] Prinz G A 1999 *J. Magn. Magn. Mater.* **200** 57
- [10] Lau H K and Leung C W 2008 *J. Appl. Phys.* **104** 123705
- [11] Singh H K, Khare N, Siwach P K and Srivastava O N 2000 *J. Phys. D: Appl. Phys.* **33** 921
- [12] Mooney J B and Radding S B 1982 *Annu. Rev. Mater. Sci.* **12** 81
- [13] Okuyama K and Lengoro I W 2003 *Chem. Eng. Sci.* **58** 537
- [14] Che S, Sakurai O, Shinozaki K and Mizutani N 1998 *J. Aerosol. Sci.* **29** 271
- [15] Todorovska R, Petrova N, Todorovsky D and Groudeva-Zotova St 2006 *Appl. Surf. Sci.* **252** 3441
- [16] Patil P S 1999 *Mater. Chem. Phys.* **59** 185 and references therein
- [17] Berger H L 1998 *Ultrasonic Liquid Atomization: Theory and Application* (Hyde Park, NY: Partridge Hill)
- [18] Rodríguez-Carvajal J 1993 *Physica B* **192** 55
- [19] Zhang Y B, Li S, Sun C Q and Gao W 2003 *Mater. Sci. Eng. B* **98** 54
- [20] Klug H P and Alexander L E 1974 *X-Ray Diffraction Procedures* (New York: Wiley)
- [21] Lopez-Quintela M A, Hueso L E, Rivas J and Rivadulla F 2003 *Nanotechnology* **14** 212
- [22] Balcells L, Fontcuberta J, Martínez B and Obradors X 1998 *Phys. Rev. B* **58** R14697
- [23] Simmons J G 1963 *J. Appl. Phys.* **34** 1793
- [24] Gupta A, Gong G Q, Xiao G, Duncombe P R, Lecœur P, Trouilloud P, Wang Y Y, Dravid V P and Sun J Z 1996 *Phys. Rev. B* **54** R15629